



TECHNICAL ARTICLE

Easy-Made Setup for High-Temperature (Up to 1100 °C) Electrochemical Impedance Spectroscopy

Mariusz Radtke and Christian Hess

Submitted: 22 September 2021 / Revised: 27 November 2021 / Accepted: 6 January 2022 / Published online: 23 February 2022

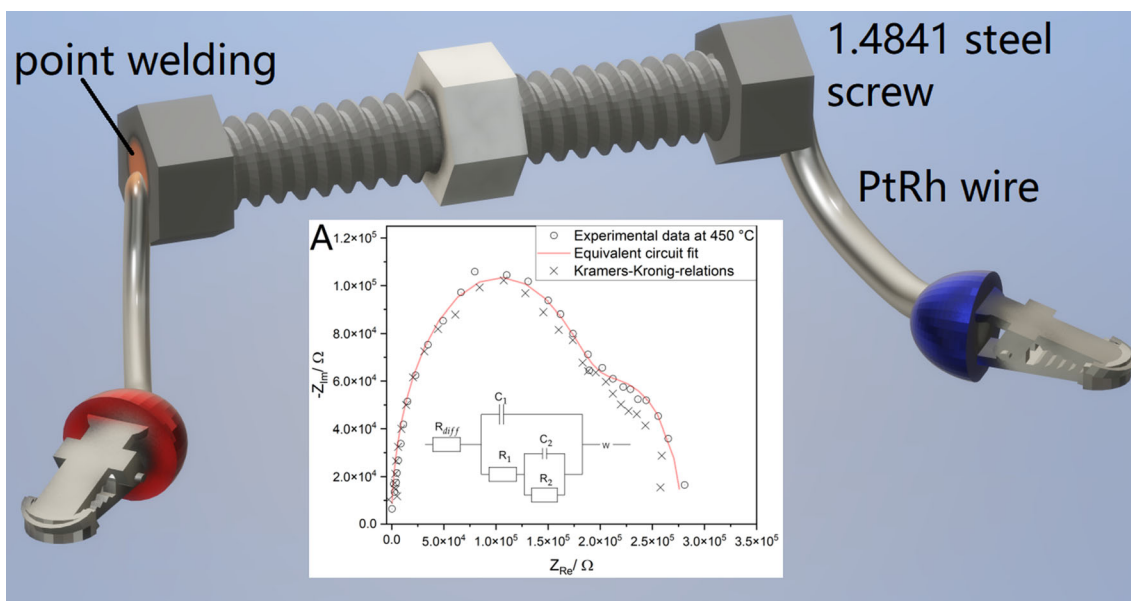
In the following communication, we report an easy-to-assemble Swagelok-like setup for high-temperature electrochemical impedance spectroscopy with good reproducibility based on robust 1.4114 steel 10M screws joined by non-conductive ceramics- Al_2O_3 . We analyze the sample materials for electrochemical merits (activation energy, charge-carrier density and flatband potential) of well-known standards such as yttria-stabilized zirconia with 8 mol.% Y_2O_3 (8YSZ), CeO_2 and In_2O_3 . The material's data are compared with literature data performed on a standard impedance analyzer within a casual high-temperature commercial cells. The symmetrical cell consists of insulating material (Al_2O_3 screw) and two steel contacts, connected by PtRh wires of thermal resistance tolerating temperatures of 2300 °C. Our high-temperature electrochemical setup is able to withstand temperatures up to 1100 °C and can be easily and mildly cleaned for repetitive usage. In addition, we present a methodology for generation of a high-temperature sintered 8YSZ ceramics and evaluate them with our setup. We analyze the internal resistances within the setup and propose a simplified option for introduction of various gas atmospheres into the sample's interior, as well as evaluate the utilization of tube furnace for simplicity. We perform equivalent circuit fitting and present an easy to implement approach for reliable high-temperature electrochemistry.

This article is an invited submission to the *Journal of Materials Engineering and Performance* selected from presentations at the symposium “Anion and Cation Transport in Materials for Energy Storage,” belonging to the area “Energy” at the European Congress and Exhibition on Advanced Materials and Processes (EUROMAT 2021), held virtually from September 12–16, 2021, and has been expanded from the original presentation.

Supplementary Information The online version contains supplementary material available at <https://doi.org/10.1007/s11665-022-06653-3>.

Mariusz Radtke and **Christian Hess**, Eduard-Zintl-Institute, Technical University of Darmstadt, Germany, Alarich-Weiss-Str. 8, 64287 Darmstadt, Germany. Contact e-mail: mariusz.radtke@tu-darmstadt.de.

Graphical abstract



Keywords ceramics, ceria, high-temperature electrochemistry, high-temperature impedance spectroscopy, indium oxide, YSZ

1. Introduction

High-temperature electrochemistry is a trending field of pivotal importance to the large-scale industry including synthetic electrolysis (e.g., NaCl production by BASF), ceramics, molten salt electrolytic metallurgy (e.g., due to the excellent conductivity of the molten media), heat transfer fluidics (HTF), thermal energy storage (TES), and electrical energy storage (EES, e.g., high-temperature fluorine salts) (Ref 1-8).

One of the most interesting examples of high-temperature electrochemistry involves dielectric spectroscopy, in particular, electrochemical impedance spectroscopy (EIS) (Ref 9-12). EIS is a technique able to non-destructively investigate crucial material parameters at high temperature, such as conductivity, viscosity (acoustic impedance spectroscopy), activation energy of oxygen vacancy in, e.g., λ -oxygen sensors, resistance of the ionic transport within, e.g., porous ceramics (Mac Mullin number for solid-state electrolytes) or even the evaluation of charge-carrier density in photovoltaic materials (Mott-Schottky junctions) (Ref 13-16). The current development of high-temperature electrochemistry makes EIS therefore a lucrative and cost-effective method for evaluation of material's behavior at elevated temperatures.

The main drawback of the application of EIS at both laboratory and pilot scale is the need for a reliable system allowing to acquire the desired spectra in a dedicated span of

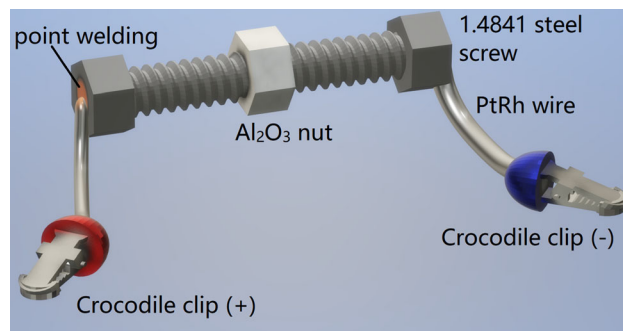


Fig. 1 Experimental cell setup based on M10 metric 1.4841 high-temperature resistant screws with Al_2O_3 nut (96% pure, 30% apparent porosity for gas permeation). The thickness of the PtRh wire is exaggerated for clarity. The cell was placed inside the tube furnace with two inlets for feeding the PtRh wires through (Carbolite, operating temperature up to 1200 °C). The crocodile clips ensure connection to the potentiostat outside the tube furnace (Figure S1, Supporting Information). The cell can be operated up to 1100 °C and is limited by the 1.4841 heat-resistant screws

alternating current (AC) frequencies (Ref 17, 18). Main parts of such a system are the signal analyzer (galvanostat for galvanostatic electrochemical impedance spectroscopy (GEIS) and potentiostat for potenti-electrochemical impedance spectroscopy (PEIS)). Most of the modern instruments (Gamry, BioLogic, Princeton Instruments, CHI, MetroOhm) utilize this bifunctionality in one setup. Another crucial part is obviously the cell containing the material for analysis, which is connected to the signal analyzer (Ref 19-22). It needs to be chemically and temperature resistant and should not or minimally and in

controlled fashion contribute to the internal resistance of the measurement, nor to the iR drop (Ref 23-25). It should also be reliable, cost-effective and easy to assemble for multiple analysis of, e.g., batches during pilot or large-scale production (Ref 26).

In order to fulfill those requirements, we propose an affordable, yet reliable and easy-to-assemble setup for high-temperature (up to 1100 °C) electrochemistry with particular emphasis on EIS. The analysis cell depicted in Fig. 1 consists of three major parts: the 1.4841 steel M10 screws with flat electrical contacts, a ceramic non-conductive alumina nut and high-temperature resistant and conductive wire connections (PtRh) point-welded by an arc discharge (300 V) to the 1.4841 steel screws. The high-porosity of the alumina nut allows to vary the gas atmosphere (e.g., vacuum, synthetic air, argon, neon). The material of interest is placed within a nut of well-defined geometry and is brought to contact with 1.4841 high-temperature-resistant steel from both sides. This allows to avoid the necessity of conductive film deposition by DC sputtering or physical vapor deposition (PVD) on the, e.g., ceramic materials

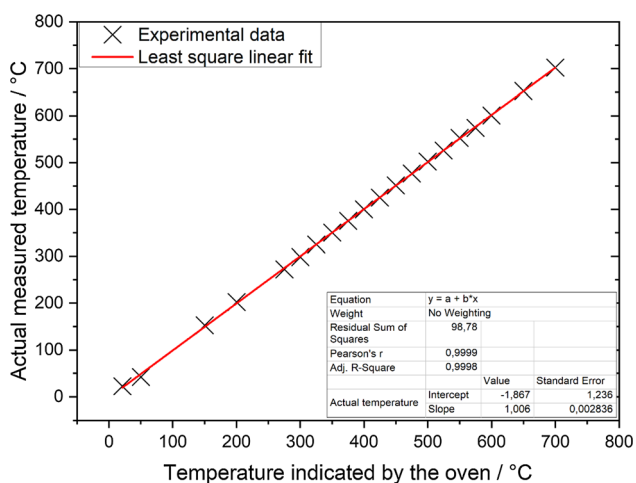
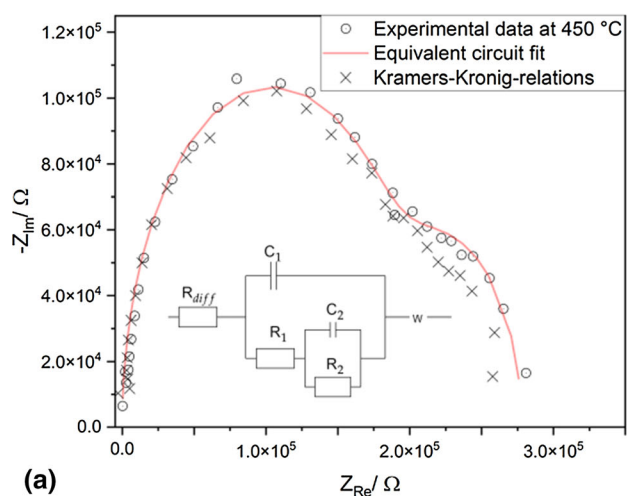


Fig. 2 Results of the temperature calibration of the cell interior



in order to create electric contact, which is often the case for laboratory-scale research. The so-prepared Swagelok-type cell may then be placed in a tube furnace with the desired gas type and flow (Fig. 2, inset A), which allows to perform electrochemical analysis.

This contribution investigates the obtained electrochemical merits on standard materials (8% yttria-stabilized zirconium oxide; 8YSZ oxygen gas sensor and catalytic RedOx-active oxide such as CeO_2 and In_2O_3), as well as research-type sintered 8YSZ ceramics. The obtained results are compared with the literature, and the potential of using the simplified Swagelok-type cell approach is discussed.

2. Materials and Methods

Electrochemical measurements of staircase potentiodynamic electrochemical impedance spectroscopy (SPEIS) were acquired with a BioLogic VSP potentiostat (France) equipped with PC-controlled EC-Lab software (version 11.33) and were performed in single sine mode in a 1MHz-1mHz frequency range. Mott-Schottky analysis was acquired in -1.5 to $+1.5$ V versus open circuit potential (OCP) range with 1500 potential steps (dE 2 mV), 10 mV sinus amplitude and 6 points per decade of frequency in logarithmic spacing with 2 measurements per set used for signal averaging. Each SPEIS spectrum was validated by Kramers-Kronig relations and numerically fitted by a Z-fit procedure with details emphasized in the text. The custom-made standardized 10M screw threads were prepared according to the standard of ISO 10642 out of steel type 1.4841 (temperature inertness till 1150 °C in air under standard conditions). PtRh wires (250 μm thick as confirmed by digital optical microscopy and of 99.9% purity, as confirmed by X-ray photoelectron spectroscopy, each 15 cm long) were point-welded to the screws in house by an arc discharge. The PtRh contribution to the Nyquist plots were neutralized by the iR drop determination, as only the electrode resistance was affected during the measurement. Standard alligator-clips were placed at the end of the wires for connecting the signals to the

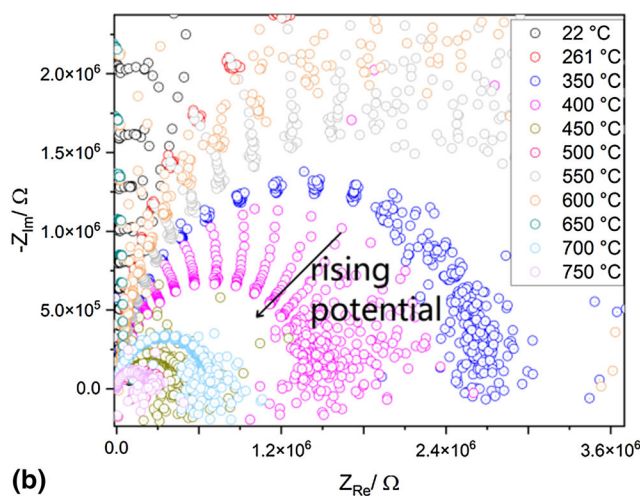


Fig. 3 Representative image of standard spectra of commercial powder In_2O_3 analyzed in an extended temperature range under non-inert atmosphere, with the RedOx reaction showing reduced (semi-circle at lower frequencies) and pristine material (semi-circle at higher frequencies) with clearly visible grain boundary. The Hilbert transforms of the impedance signals yielded $\langle \Delta|Z| \rangle = 6.7\%$ and $\langle \Delta \text{Phase}(Z) \rangle = 4.8\%$, which is comparable with the accuracy provided by commercial analyzers (Ref 37)

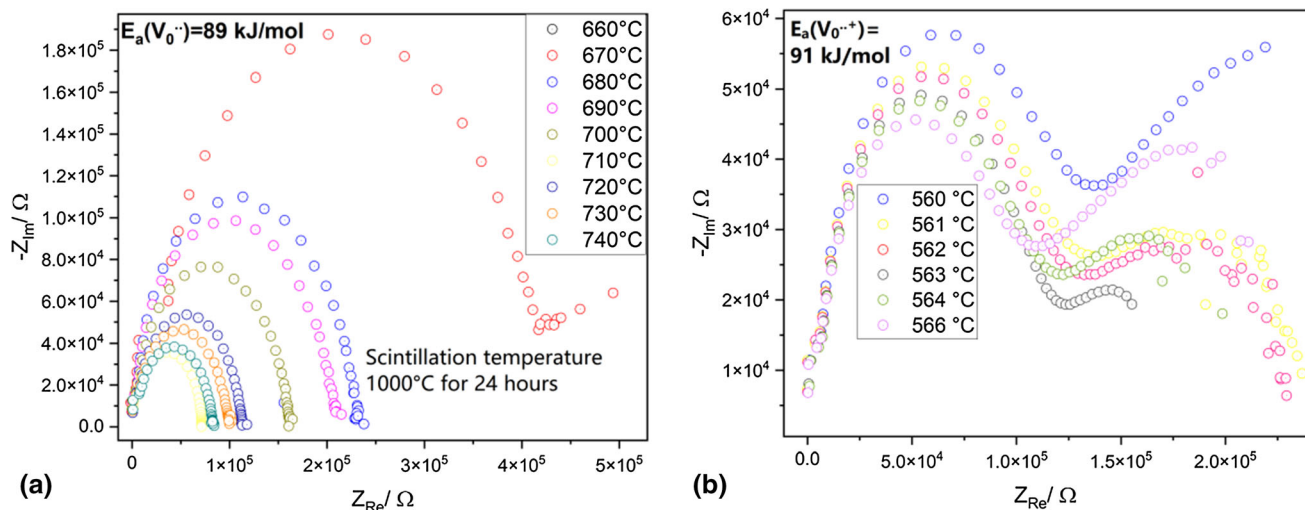


Fig. 4 Research-grade sintered 8YSZ (a) compared to the standard purchased materials (b) under oxygen flow

Table 1 Electrochemical merits of the measured samples compared to literature values

Electrochemical merit	Sample	Literature value	
Activation energy kJ/mol	CeO ₂ ¹	91.66	123.5 (Ref 31)
	In ₂ O ₃ ²	136.98	134.8 (Ref 32)
	8YSZ	83.21	82.7 (Ref 33)
	Synthesized 8YSZ	89.01	82.7 (Ref 34)
	Synthetic 8YSZ under O ₂ flow	91.05	82.7 (Ref 35)
Charge-carrier concentration cm ⁻³	CeO ₂	1.54E16	6E17 (Ref 52)
	In ₂ O ₃	8.25E16	3.8E17 (Ref 53)
	8YSZ ³	2.5E17	2E18 (Ref 51)
	Synthesized 8YSZ ⁴	4.7E16	2E18 (Ref 51)
	Synthetic 8YSZ under O ₂ flow ⁵	5.4E14	2E18 (Ref 53)
Flatband potential V versus NHE	CeO ₂	- 1.23	- 0.43 (Ref 52)
	In ₂ O ₃	0.65	0.85 (Ref 53)
	8YSZ	0.42	... ⁶
	Synthesized 8YSZ	0.89	... ⁶
	Synthetic 8YSZ under O ₂ flow	0.85	... ⁶

¹At 350 °C, powder

²At 350 °C, powder

³At 660 °C, pellet

⁴At 560 °C, pellet

⁵At 560 °C, pellet

⁶Data not reported in the literature

potentiostat. The internal resistance of the PtRh wire was established as less than 0.1 mOhm and is therefore excluded from the calculation of the electrochemical merits. The conductivity was calibrated using alomel (99.9% purity, in-house source). The dihedral-width M10 nuts were purchased from Misumi, Japan (CA/NN-M10), which are composed of 96% alumina (with rest 4% of calcium oxide impurities, as established by X-Ray photoelectron spectroscopy in house) and are of 30% apparent porosity. The tube furnace from Carbolite Furnaces Ltd &02-3216P1 (Type MTF 12/25 A Figure S1) with internal controller was employed (Figure S1, Supporting Information). The temperature within the nut was calibrated as opened (one side left unclosed with steel screw) after 45

minutes from reaching the measurement temperature by the K-thermocouple of +/- 1.1 °C measurement certainty and 35 μV/K Seebeck coefficient, to which all temperature measurements in text are referred (Fig. 2). CeO₂, In₂O₃ and the 8YSZ powders were purchased from Sigma-Aldrich/Merck, Germany. The 8YSZ scintillated pellet was prepared by pressing 100 mg material in a 10-mm piston under 10 tons of hydraulic pressure and subsequent scintillation at 1000 °C for 24 hours under atmospheric air. The commercial 8YSZ pellet fitting 10M metric screw was purchased from Keramik GmbH, Germany. The gas flow into the cell was introduced by inserting the inlets and outlets to the Carbolite tube furnace (Figure S1). The gas flow in sccm was controlled by a home-build Hg manometer.

The point welding was performed by a direct current (DC) arc discharge at 300 V, without the use of any external metals.

3. Results and Discussion

We present a design of the measurement cell, calibration of the tube furnace temperature and results for impedance characterization of the materials 8YSZ, CeO₂, In₂O₃ and self-sintered experimental 8YSZ. We estimate the activation energies, flatband potentials and internal resistances of the cell based on equivalent circuit analysis according to the standardized Z-fit numerical procedure. We present the experimental measurement data up to 750 °C and estimate the capability of measurements up to 1100 °C in order to evaluate the cell stability.

3.1 Cell Design and its Validation

In the first step, the cell was assembled according to Fig. 1. PtRh wires were attached to crocodile clips and the measurement cell setup could be compared to the 2-probe measurement of a typical 2-electrode cell. The only contribution of the conductivity is the material under investigation, as Al₂O₃ is not conductive also at elevated temperature. The potentially occurring perturbation arising from the wiring was removed by application of PtRh wire with minimal self-resistance. The quality of PtRh was carefully evaluated by means of XPS spectroscopy. The thermal resistance up to 2300 °C and excellent electrical conductivity of this alloy have allowed for non-disturbed measurements.

The relatively large porosity of the alumina nut has allowed for introduction of various gaseous environments into the interior of the investigation area. An example of such a measurement under 20 sccm of oxygen flow at elevated temperatures is presented in Fig. 4, inset B, for yttria-stabilized zirconia with 8 mol.% Y₂O₃ (8YSZ), bearing two vacancies for each unit cell, according to the equation in the Kröger–Vink notation: Y₂O₃(s) → 2Y_{Zr}⁺ + 3O_O^x + 3V_O[·], which further leads to pressure-dependent saturation of vacancies by oxygen: O₂(g) → 1/2 O₂(g) + 2e[·] + V_O[·]. Here, the [·] means the negative charge, while ⁺ is the positive charge. V_O[·] is the vacancy replacing oxygen, and x stands for the charge-neutrality. The presence of oxygen vacancies is strongly suggested, as based on the activation energy, which was calculated to be 89.01 kJ/mol (0.92 eV) for the synthesized 8YSZ, 83.21 kJ/mol (0.86 eV) for the commercial 8YSZ ceramic ring (GmbH, Germany), 91.66 kJ/mol (0.92 eV) for CeO₂ and 136.98 kJ/mol (1.38 eV) for In₂O₃ (Table 1). Owing to the various concentrations of oxygen vacancies, which was additionally investigated by means of staircase potentiostatic-impedance spectroscopy (SPEIS) and the Mott–Schottky equation (Eq 2), the value of the activation energy was established to depend on the chemical environment (Ref 27). The results of the activation energy, charge-carrier concentration and flatband potential calculations are gathered in Table 1. We note that the dielectric constants needed for the calculations of the concentrations of active species were calculated according to the procedures reported in the literature; in our case, we restrict ourselves to fixed temperatures with smallest values of resistance, as judged by a Z-fit of the equivalent circuits (Ref 28, 29).

Figure 2 shows a representative plot for the Al₂O₃ nut interior temperature calibration within the opened measurement cell placed within the tube furnace. Owing to the uniform thermal convection within the tube furnace, the nut interior measured with one side open (i.e., with one screw left out) has proven the accuracy of the temperature readout of the furnace display and of the K-element thermocouple temperature readout placed within the cell's interior.

3.2 Measurements of Standards

In order to assess the applicability of simple measurement cell in Fig. 1, we have performed a temperature-dependent determination of oxygen vacancies within CeO₂, In₂O₃, commercial 8YSZ and self-made 8YSZ under various gas atmospheres. By applying the Arrhenius equation:

$$\ln \sigma = \ln A - \ln(E_a/RT) \quad (\text{Eq 1})$$

and the Mott–Schottky equation:

$$1/C^2 = 2/(\epsilon\epsilon_0 A^2 e N_D)(V_{\text{vs NHE}} - V_{\text{FB}} - k_B T/e) \quad (\text{Eq 2})$$

where σ is the conductivity, A the Arrhenius constant, E_a the activation energy, R the universal gas constant, T the temperature, and C is the capacitance, ϵ and ϵ_0 are the dielectric constant and permittivity in vacuum, k_B is the Boltzmann constant, A the electrode surface area, e the number of electrons transferred (assumed as 1), N_D the charge-carrier density (in cm⁻³), V is the measured potential against the normal hydrogen electrode (NHE, in Volt), and V_{FB} is the flatband potential (in Volt).

According to the proposed hopping mechanism of conductivity in the literature, which depends on the amount of available and addressable (at the given temperature) oxygen vacancies, the saturation of those by gas flow leads to differences in impedance spectra and is a well-known phenomenon (Ref 30). Our approach was to evaluate the Al₂O₃ porosity in order to observe the effect of oxygen saturation. The experimental results for oxygen flow (20 sccm) are shown in Fig. 4, insets A/B.

The measurements of commercial standards are in agreement with the literature (Ref 31–35). The equivalent circuit modeling is exemplary shown in the Fig. 3, inset A, as a magnified cut-out from the cumulative assembly of EIS spectra in the inset B. The spectra show good agreement with the theoretically obtainable results (error analysis of the Z-fit $\chi^2/Z = 0.35$), as judged by the 6.7% error yielded by the Kramers–Kronig relations (KK relations). The KK analysis represents the mathematical dependence of the imaginary and real parts of the impedance, therefore proving the application potential of the proposed high-temperature measurement system (Ref 36).

The conductivity of CeO₂ and In₂O₃ owing to the hopping mechanism was evaluated and found to be in good comparison with the literature data (Ref 38, 39). We have observed the accessibility of oxygen vacancies to vary at different temperatures, but considered a temperature of 350 °C for both CeO₂ and In₂O₃ in order to compare the charge-carrier density with literature values (Ref 31–35). The respective Arrhenius plots for CeO₂, In₂O₃ and YSZ (both synthesized and commercial) can be found in the Supporting Information.

The substitution of Ce⁴⁺ in ceria and In³⁺ in indium oxide by foreign elements due to the implantation or respective sample preparation (e.g., electrospinning) results in an increased

amount of oxygen vacancies, which are treated as the main source of the charge-carriers (Ref 40). Many of the vacancies will nevertheless be intrinsically built into the structure as point defects, which consequently leads to an improved conductivity (Ref 41). The different accessibility of oxygen vacancies is translated to charge-carrier densities and is not to be referred to structural changes, as, e.g., ceria exhibiting a fluorite Fm3m space group up to its melting point at 2477 °C, but rather to the bulk activation energy needed per mol unit of the material under investigation (Ref 42, 43). For example, the charge-carrier density of In₂O₃ can vary, as it depends on the amount of reduced material, which occurs due to the thermal RedOx reduction reaction: $2\text{In}_2\text{O}_3 \rightarrow 4\text{In}^0 + 3\text{O}_2$, meaning that the material's chemistry is involved in a large bundle of parameters influencing the conductivity. In the case of oxide materials, this may vary from batch to batch (Ref 43, 44).

3.3 Measurement of Experimental Research Samples

In order to investigate the potential of the proposed setup, we have performed a real-run test of the research-type prepared samples. The 8YSZ powder was sintered under air for 24 hours at 1000 °C prior to pelletization as described in the materials and methods section. The translucent ceramic pellet was carefully placed inside the measurement cell and brought into the tube furnace. We have observed much higher temperature activity of the sample at 660 °C, as manifested by the generation of the semi-circle in the Nyquist plot and therefore the observed temperature-dependent conductivity. The results aiming for a comparison of the merits obtained by our cell with literature values are gathered in Table 1. Figure 4 shows the applicability of the cell for measurements during respective gas treatments. The spectra in A and B show different temperatures, while only in the range of 560-566 °C the peculiar generation of the second semi-circle was observed, which was attributed to the phase transition within the monoclinic 8YSZ system to the tetragonal system (Ref 54). Interestingly, this phase transition behavior was observed only under oxygen atmosphere. Further discussion of this effect is nevertheless outside of scope of this article and we refer to the reader to the comprehensive review of that matter in the literature (Ref 54).

The peculiarity of ceramic solid and oxygen gas interaction is still a matter of research, as conductivity (both electrical and ionic) measurements at higher temperatures are considered to be challenging (Ref 45). The dependence of the gas atmosphere on the 8YSZ conductivity (specified in this study by a gas pressure of 1 atm and a flow of 20 sccm) and especially on the oxygen vacancies saturation is manifested by the presence of the charges in the bulk of the material, which causes creation of holes within CeO₂ and In₂O₃. The exact character of holes and the creation of localized Frenkel exciton states within the 8YSZ, as well as their exact position and contribution to the final states of the Bloch-conduction band, are not fully understood yet and are currently a matter of intensive computational studies (Ref 46-49). In case of the data presented in Table 1, the conductivity of 8YSZ varies strongly with the atmosphere, while the position of relative to the conduction band and easily obtainable flatband may provide additional merits explaining the accessibility of excitons and their influence on the conductivity (Ref 50). The possibility of more careful temperature control should provide better insight into the quantum properties of ceramics under investigation within our system.

4. Conclusions

In this study, we have presented an easy method for reliable measurements of high-temperature impedance spectroscopy in a cell of well-defined geometry, easy availability of the assembly materials and high durability. The cell consists of 1.4841 10M steel screws with temperature resistance up to 1150 °C, alumina (96% Al₂O₃) and PtRh connectors. We have performed analysis of electrochemical merits like activation energy of oxygen vacancies in ceria, In₂O₃ and yttria-stabilized zirconium oxide, their charge-carrier concentration and flatband potential. We have established that the amount of charge transfer concentration varies with temperature, which we refer to as the activation energy needed to successfully activate the active centers and we discussed the availability of Frenkel excitons potentially contributing to the conductivity. The theory of flatband was referred to the position of the Bloch-conduction band in order to demonstrate the possibility of performing investigations of quantum electronic structure of both powders and pellets. After characterization of the commercial standards, we have demonstrated a possibility of investigation of research-grade materials, such as self-prepared 8YSZ. We also shown the influence of gas atmosphere on the impedance measurement due to the large 30% porosity of the alumina used as the powder/pellet vessel. In conclusion, our approach can be used in any tube furnace of adequate size and our normalized approach of the cell makes high-temperature impedance measurements a straightforward, reproducible and highly accurate task.

Author Contributions

Conceptualization, M. Radtke; methodology and validation, M.R.; formal analysis, M.R.; investigation, M.R.; resources, C.H.; data curation, M.R.; writing—original draft preparation, M.R.; writing—review and editing, M.R. and C. H.; visualization, M.R.; project administration, C.H.; funding acquisition, C.H.

Funding

Open Access funding enabled and organized by Projekt DEAL. We acknowledge the funding provided by Deutsche Forschungsgemeinschaft (DFG, HA 6128/6-1).

Conflict of interest

The authors declare no conflict of interest.

Open Access

This article is licensed under a Creative Commons Attribution 4.0 International License, which permits use, sharing, adaptation, distribution and reproduction in any medium or format, as long as you give appropriate credit to the original author(s) and the source, provide a link to the Creative Commons licence, and indicate if changes were made. The images or other third party material in this article are included in the article's Creative Commons licence, unless indicated otherwise in a credit line to the material. If

material is not included in the article's Creative Commons licence and your intended use is not permitted by statutory regulation or exceeds the permitted use, you will need to obtain permission directly from the copyright holder. To view a copy of this licence, visit <http://creativecommons.org/licenses/by/4.0/>.

References

1. T. Liu, X. Zhang, L. Yuan, and J. Yu, A Review of High-Temperature Electrochemical Sensors Based On Stabilized Zirconia, *Solid State Ion.*, 2015, **283**, p 91–102.
2. A. Weiß, S. Schindler, S. Galbati, M.A. Danzer, and R. Zeis, Distribution of Relaxation Times Analysis of High-Temperature PEM Fuel Cell Impedance Spectra, *Electrochim. Acta*, 2017, **230**, p 391–398.
3. X. Lin, M. Salari, L.M.R. Arava, P.M. Ajayan, and M.W. Grinstaff, High Temperature Electrical Energy Storage: Advances, Challenges, and Frontiers, *Chem. Soc. Rev.*, 2016, **45**, p 5848–5887.
4. W. Ding, A. Bonk, and T. Bauer, Corrosion Behavior of Metallic Alloys in Molten Chloride Salts for Thermal Energy Storage in Concentrated Solar Power Plants: A Review, *Front. Chem. Sci. Eng.*, 2018, **12**(3), p 564–576.
5. N.Q. Minh, Extraction of Metals by Molten Salt Electrolysis: Chemical Fundamentals and Design Factors, *JOM*, 1985, **37**(1), p 28–33.
6. G.G. Botte, Electrochemical Manufacturing in the Chemical Industry, *Interface*, 2014, **23**(3), p 49–55.
7. S. Upadhyay, High Temperature Impedance Spectroscopy of Barium Stannate, BaSnO₃, *Bull. Mater. Sci.*, 2013, **36**(6), p 1019–1036.
8. M.A. Nowroozi, K. Wissel, M. Donzelli, N. Hosseinpourkavaz, S. Plana-Ruiz, U. Kolb, R. Schoch, M. Bauer, A.M. Malik, J. Rohrer, S. Ivlev, F. Kraus, and O. Clemens, High Cycle Life All-Solid-State Fluoride Ion Battery with La₂NiO_{4+d} High Voltage Cathode, *Commun. Mater.*, 2020, **1**(1), p 27.
9. H. de Castilla, P. Belanger, and R.J. Zednik, High Temperature Characterization Of Piezoelectric Lithium Niobate Using Electrochemical Impedance Spectroscopy Resonance Method, *J. Appl. Phys.*, 2017, **122**(24), p 244103.
10. V. Balasubramani, S. Chandraleka, T.S. Rao, R. Sasikumar, M.R. Kuppusamy, and T.M. Sridhar, Review—Recent Advances in Electrochemical Impedance Spectroscopy Based Toxic Gas Sensors Using Semiconducting Metal Oxides, *J. Electrochem. Soc.*, 2020, **167**(3), p 037572.
11. S. Sahlin, S.S. Araya, S.J. Andreasen, and S. Kær, Electrochemical Impedance Spectroscopy (EIS) Characterization of Reformate- Operated High Temperature PEM Fuel Cell Stack, *Int. J. Energy Res.*, 2017, **1**(1), p 20–40.
12. A.R.C. Bredar, A.L. Chown, A.R. Burton, and B.H. Farnum, Electrochemical Impedance Spectroscopy of Metal Oxide Electrodes for Energy Applications, *ACS App. Ener. Mat.*, 2020, **3**(1), p 66–98.
13. E. Ponomarev, and L. Peter, A Comparison of Intensity Modulated Photocurrent Spectroscopy and Photoelectrochemical Impedance Spectroscopy in a Study of Photoelectrochemical Hydrogen Evolution at p-InP, *J. Electroanal. Chem.*, 1995, **397**(1), p 45–52.
14. A. Nechache, M. Cassir, and A. Ringuedé, Solid Oxide Electrolysis Cell Analysis by Means of Electrochemical Impedance Spectroscopy: A Review, *J. Power Sources*, 2014, **258**, p 164–181.
15. N. Meddings, M. Heinrich, F. Overney, J.-S. Lee, V. Ruiz, E. Napolitano, S. Seitz, G. Hinds, R. Raccichini, M. Gaberšček and J. Park, Application of Electrochemical Impedance Spectroscopy to Commercial Li-ion Cells: A Review, *J. Power Sources*, 2020, **480**, p 228742.
16. L.A. Middlemiss, A.J. Rennie, R. Sayers, and A.R. West, Characterisation of Batteries by Electrochemical Impedance Spectroscopy, 4th Annual CDT Conference in Energy Storage and its Applications, *Ener. Rep.*, 2020, **6**, p 232–241.
17. A. Bogomolova, E. Komarova, K. Reber, T. Gerasimov, O. Yavuz, S. Bhatt, and M. Aldissi, Challenges of Electrochemical Impedance Spectroscopy in Protein Biosensing, *Anal. Chem.*, 2009, **81**(10), p 3944–3949.
18. J.F. Silva, A.C. Dias, P. Araújo, C.M.A. Brett, and A. Mendes, Electrochemical Cell Design for the Impedance Studies of Chlorine Evolution at DSA® anodes, *Rev. Sci. Inst.*, 2016, **87**(8), p 085113.
19. B.-Y. Chang, and S.-M. Park, Electrochemical Impedance Spectroscopy, *Annu. Rev. Anal. Chem.*, 2010, **1**, p 207–229.
20. A. Al-Ali, and B. Maundy, *Design and Implementation of Portable Impedance Analyzers*, Springer, Cham, 2019
21. U.G. Kyle, I. Bosaeus, A.D. De Lorenzo, P. Deurenberg, M. Elia, J.M. Gómez, B.L. Heitmann, L. Kent-Smith, J.-C. Melchior, M. Pirlich, H. Scharfetter, A.M. Schols, and C. Pichard, Bioelectrical Impedance Analysis—Part I: Review of Principles and Methods, *Clin. Nut.*, 2004, **23**(5), p 1226–1243.
22. B. Igarashi, T. Christensen, E.H. Larsen, N.B. Olsen, I.H. Pedersen, T. Rasmussen, and J.C. Dyre, An Impedance-Measurement Setup Optimized for Measuring Relaxations of Glass-Forming Liquids, *Rev. Sci. Inst.*, 2008, **79**(4), p 045106.
23. T. Pajkossy, and G. Mészáros, Connection of CVs and Impedance Spectra of Reversible Redox Systems, as Used for the Validation of a Dynamic Electro-Chemical Impedance Spectrum Measurement System, *J. Solid State Electrochem.*, 2020, **24**(11), p 2883–2889.
24. S. Anantharaj, and S. Noda, Appropriate Use of Electrochemical Impedance Spectroscopy in Water Splitting Electrocatalysis, *ChemElectroChem*, 2020, **7**(10), p 2297–2308.
25. B.A. Lambie, C. Brennan, J. Olofsson, O. Orwar, and S.G. Weber, Experimentally Determining the iR Drop in Solution at Carbon Fiber Microelectrodes with Current Interruption and Application to Single-Cell Electroporation, *Anal. Chem.*, 2007, **79**(10), p 3771–3778.
26. J. Cen, M. Vukas, G. Barton, J. Kavanagh, and H. Coster, Real time Focusing Monitoring with Electrical Impedance Spectroscopy, *J. Membr. Sci.*, 2015, **484**, p 133–139.
27. M. Todorova, and J. Neugebauer, Identification Of Bulk Oxide Defects in an Electrochemical Environment, *Faraday Discuss.*, 2015, **180**, p 97–112.
28. V.V. Brus, A.K.K. Kyaw, P.D. Maryanchuk, and J. Zhang, Quantifying Interface States and Bulk Defects in High-Efficiency Solution-Processed Small-Molecule Solar Cells by Impedance and Capacitance Characteristics, *Prog. Photovolt. Res. Appl.*, 2015, **23**(11), p 1526–1535.
29. S.M. Sze, and K.K. Ng, *Physics of Semiconductor Devices*, Wiley-Interscience, Hoboken, 2007
30. H. Jeon, Z. Bi, W.S. Choi, M.F. Chisholm, C.A. Bridges, M.P. Paranthaman, and H.N. Lee, Orienting Oxygen Vacancies for Fast Catalytic Reaction, *Adv. Mater.*, 2013, **25**(44), p 6459–6463.
31. D. Puente-Martínez, J. Diaz-Guillén, S. Montemayor, J. Diaz-Guillén, O. Burciaga-Díaz, M. Bazaldúa-Medellín, M. Diaz-Guillén and A. Fuentes, High Ionic Conductivity in CeO₂ Soft Solid Electrolytes; Effect of Dy Doping on their Electrical Properties, *Int. J. Hydrog. Energy*, 2020, **45**(27), p 14062–14070.
32. In₂O₃ activation energy: Datasheet from “PAULING FILE Multinaries Edition - 2012” in Springer- Materials (<https://materials.springer.com/isp/physical-property/docs/pppfc7238df8f9fdb7325fef63821437fd>), accessed November 15th 2021
33. C. Ahamer, A.K. Opitz, G.M. Rupp, and J. Fleig, Revisiting the Temperature Dependent Ionic Conductivity of Ytria Stabilized Zirconia (YSZ), *J. Electrochem. Soc.*, 2017, **164**(7), p F790–F803.
34. N. Masó, and A.R. West, Electronic Conductivity in Ytria-Stabilized Zirconia Under a Small DC Bias, *Chem. Mater.*, 2015, **27**(5), p 1552–1558.
35. J.-H. Lee, S. Yoon, B.-K. Kim, J. Kim, H.-W. Lee, and H.-S. Song, Electrical Conductivity and Defect Structure of Ytria-Doped Ceria-Stabilized Zirconia, *Solid State Ion.*, 2001, **144**(1), p 175–184.
36. C. You, M.A. Zabara, M.E. Orazem, and B. Ulgut, Application of the Kramers-Kronig Relations to Multi-Sine Electrochemical Impedance Measurements, *J. Electrochem. Soc.*, 2020, **167**(2), p 020515.
37. M. Hahn, S. Schindler, L.-C. Triebes, and M.A. Danzer, Optimized Process Parameters for a Reproducible Distribution of Relaxation Times Analysis of Electrochemical Systems, *Batteries*, 2019, **5**(2), p 43.
38. B. Wang, B. Zhu, S. Yun, W. Zhang, C. Xia, M. Afzal, Y. Cai, Y. Liu, Y. Wang, and H. Wang, Fast Ionic Conduction in Semiconductor CeO₂-δ electrolyte Fuel Cells, *NPG Asia Mater.*, 2019, **11**(1), p 51.
39. C. Mariappan, E. Prabhu, K. Gnanasekar, V. Jayaraman, T. Gnanasekaran, Impedance spectroscopy analysis of In₂O₃ thin film gas sensor, in: 2012 1st International Symposium on Physics and Technology of Sensors (ISPTS-1), 2012, p 200–203

40. M. Mogensen, N.M. Sammes, and G.A. Tompsett, Physical, Chemical and Elec-Trochemical Properties of Pure and Doped Ceria, *Solid State Ion.*, 2000, **129**(1), p 63–94.
41. Effects of rare-earth doping on the ionic conduction of CeO₂ in solid oxide fuel cells, *Ceramics International*, 2018, **44**, 4, p 3707–3711
42. Z. Cai, B. Song, L. Li, Z. Liu, and X. Cui, Effects of CeO₂ on Viscosity, Structure, and Crystallization of Mold Fluxes for Casting Rare Earths Alloyed Steels, *Metals*, 2019, **9**(3), p 333.
43. H. Zhu, C. Yang, Q. Li, Y. Ren, J.C. Neuefeind, L. Gu, H. Liu, L. Fan, J. Chen, J. Deng, N. Wang, J. Hong, and X. Xing, Charge Transfer Drives Anomalous Phase Transition in Ceria, *Nat. Commun.*, 2018, **9**(1), p 5063.
44. H.-I. Ji, T.C. Davenport, C.B. Gopal, and S.M. Haile, Extreme High Temperature Redox Kinetics in Ceria: Exploration of the Transition from Gas-Phase to Material-Kinetic Limitations, *Phys. Chem. Chem. Phys.*, 2016, **18**, p 21554–21561.
45. S. Ma, M. Jiang, P. Tao, C. Song, J. Wu, J. Wang, T. Deng, and W. Shang, Temperature Effect and Thermal Impact in Lithium-Ion Batteries: A Review, *Prog. Nat. Sci. Mat. Int.*, 2018, **28**(6), p 653–666.
46. M.A. Parkes, D.A. Tompsett, M. d’Avezac, G.J. Offer, N.P. Brandon, and N.M. Harrison, The Atomistic Structure of Yttria Stabilised Zirconia at 6.7 mol.%: an ab Initio Study, *Phys. Chem. Chem. Phys.*, 2016, **18**, p 31277–31285.
47. R. Buczko, G. Duscher, S.J. Pennycook, and S.T. Pantelides, Excitonic Effects in Core-Excitation Spectra of Semiconductors, *Phys. Rev. Lett.*, 2000, **85**, p 2168–2171.
48. G. Stapper, M. Bernasconi, N. Nicoloso, and M. Parrinello, Ab initio Study of Structural and Electronic Properties of Yttria-Stabilized Cubic Zirconia, *Phys. Rev. B*, 1999, **59**, p 797–810.
49. G. Marcaud, S. Serma, K. Panaghiotis, C. Alonso-Ramos, X.L. Roux, M. Berciano, T. Maroutian, G. Agnus, P. Aubert, A. Jollivet, A. Ruiz-Cardad, L. Largeau, N. Isac, E. Cassan, S. Matzen, N. Dubreuil, M. Rérat, P. Lecoeur, and L. Vivien, Third-order Nonlinear Optical Susceptibility of Crystalline Oxide Yttria-Stabilized Zirconia, *Photon. Res.*, 2020, **8**(2), p 110–120.
50. D. Duffy, S. Daraszewicz, and J. Mulroue, Modelling the Effects of Electronic Excitations in Ionic-Covalent Materials, Nuclear Instruments and Methods, *Phys. Res. B*, 2012, **277**, p 21–27.
51. N. Nicoloso, A. Löbert, W. Weppner, and A. Rabenau, Optoelectrochemical Study of Minority Charge Carriers in YSZ, *Solid State Ion.*, 1990, **40–41**, p 320–323.
52. Z.U. Abideen, F. Teng, W. Gu, Z. Yang, A. Zhang, F. Zhao, and A.H. Shah, Enhanced Visible Light Photocatalytic Activity of CeO₂@Zn_{0.5}Cd_{0.5}S by facile Ce(IV)/Ce(III) cycle, *Arab. J. Chem.*, 2020, **13**(2), p 4198–4209.
53. C. Chen, J. Moir, N. Soheilnia, B. Mahler, L. Hoch, K. Liao, V. Hoepfner, O’Brien, C. Qian, L. Hes, G. A. Ozin, Morphology-controlled In₂O₃ nanostructures enhance the performance of photoelectrochemical water oxidation, *Nanoscale*, 2015, **7**, p 3683–3693
54. P.K. Schelling, S.R. Phillpot, and D. Wolf, Mechanism of the Cubic-to-Tetragonal Phase Transition in Zirconia and Yttria-Stabilized Zirconia by Molecular-Dynamics Simulation, *J. Am. Ceram. Soc.*, 2001, **84**, p 1609–1619.

Publisher's Note Springer Nature remains neutral with regard to jurisdictional claims in published maps and institutional affiliations.